An Improved Model Predictive Control Method Using Optimized Voltage Vectors for Vienna Rectifier With Fixed Switching Frequency

Chang Liu, *Student Member, IEEE*, Xiangyang Xing, *Member, IEEE*, Chunshui Du, *Member, IEEE*, Boxue Zhang, Chenghui Zhang, *Senior Member, IEEE*, and Frede Blaabjerg, *Fellow, IEEE*

***Abstract*—The Vienna rectifier is an attractive topology for industrial applications. In order to obtain fixed switching frequency (FSF) while maintaining lower current distortion, an improved model predictive control (MPC) method using optimized voltage vectors and switching sequences is proposed in this article. First, the space vector diagram of the Vienna rectifier is divided into six sectors according to the input currents. Then using finite-set MPC (FS-MPC), the sector can be further divided into subsectors, which reduces the number of the candidate vectors from 19 to 7 simultaneously. Second, to achieve decoupling of the neutral-point (NP) voltage balancing and current distortion, the small regions are recombined into novel N- or P-type regions to compensate for the absent vectors. More importantly, the FSF is realized by the multiple vectors determined together by the fluctuation of the NP voltage and the cost function without weighting factors, which improves the current quality and it is beneficial for filter design. Finally, based on FSF-MPC, sequence optimization between adjacent sampling periods is further considered. Compared with FSF-MPC, the improved FSF optimized (FSFO) MPC can significantly reduce the switching loss. The effectiveness of the proposed FSF- and FSFO-MPC methods is verified by simulation and experiment.**

***Index Terms*—Current distortion mitigation, fixed switching frequency model predictive control (FSF-MPC) method, fixed switching frequency optimized model predictive control (FSFO-MPC), neutral-point (NP) voltage balance, Vienna rectifier.**

I. Introduction

THE Vienna rectifier has been adopted in electric vehicle charging system and industry application due to the high efficiency and less use of switches. However, the current distortion appears when the voltage vector is changed between sectors. Furthermore, the neutral-point (NP) voltage balance and switching loss reduction should be considered simultaneously.

A number of modulation methods have been proposed for the Vienna rectifier for the current distortion mitigation, NP voltage balance, and switching loss reduction. In [1] and [2], an improved space vector modulation scheme and a hybrid control strategy are proposed to mitigate the current distortion. Nevertheless, space vector modulation is complicated. To address this issue, a zero-sequence component injection modulation method is proposed in [3] to mitigate current harmonics under the balanced or unbalanced load conditions. In [4] and [5], a sinusoidal harmonic voltage injection pulsewidth modulation (PWM) and carrier-based PWM method are proposed to mitigate the current distortion and balance the NP voltage. Besides, the loss should be considered in practice. Thus, in [6] and [7], the discontinuous PWM (DPWM) methods come up to improve the system efficiency and reduce the input current distortion.

Recently, model predictive control (MPC) has become interesting for easily achieving the multiobjective control, and it shows more advantages in fast dynamic response without using proportional-integral controller and inherent decoupling [8], [9], [10]. In essence, for MPC, it is necessary to minimize the cost function which penalizes the error between the required and predicted items and satisfy constraints imposed on process per sampling period [11]. Due to the good control performance, a large number of MPC strategies have been applied in practice [12], [13].

Nevertheless, with the growing number of converter voltage levels, the computational burden in the MPC increases exponentially. For example, for a three-phase rectifier, there are 8 (2^3) vectors in the two-level condition while 27 (3^3) vectors in the three-level case. In addition, when the multiobjective MPC strategy is conducted, weighting factors are usually introduced into the cost function. It can not only increase the computational burden, but can also be tedious to select the suitable weighting factors [13]. To improve the computational efficiency effectively, the MPC strategy based on a simplified simulated annealing is proposed in [14]. However, it optimizes the weighting factors online rather than eliminating them. The remaining weighting factors still increase the computational burden. To overcome the

Manuscript received 9 April 2022; revised 28 July 2022; accepted 28 August 2022. Date of publication 12 September 2022; date of current version 10 October 2022. This work was supported in part by the Foundation for Innovative Research Groups of National Natural Science Foundation of China under Grant 61821004, in part by the National Natural Science Foundation of China under Grant U1964207, in part by the National Natural Science Foundation of China under Grant 62222309 and Grant 62173210, and in part by the Natural Science Foundation of Shandong Province under Grant ZR2020YQ50. Recommended for publication by Associate Editor Z. Zhang. *(Corresponding author: Chenghui Zhang.)*

Chang Liu, Xiangyang Xing, Chunshui Du, Boxue Zhang, and Chenghui Zhang are with the School of Control Science and Engineering, Shandong University, Jinan 250061, China (e-mail: 202220688@mail.sdu.edu.cn; xyxing@sdu.edu.cn; duchsh@sdu.edu.cn; zhangbx@mail.sdu.edu.cn; zchui@sdu.edu.cn).

Frede Blaabjerg is with the AAU Energy, Aalborg University, DK-9220 Aalborg, Denmark (e-mail: fbl@et.aau.dk).

Color versions of one or more figures in this article are available at https://doi.org/10.1109/TPEL.2022.3205946.

Digital Object Identifier 10.1109/TPEL.2022.3205946

above-mentioned limitation, an MPC without weighting factors is proposed with computational burden reduced [15]. In [16], an improved current MPC is proposed to handle multiple control objectives. They all obtain good control performance. Nevertheless, the mentioned methods select only one space vector to track the reference voltage per sampling period, resulting in larger current ripples.

With the purpose of higher current quality, a double-vector MPC strategy for three-level inverters has been proposed in [17]. During each sampling period, two candidate vectors are used to track the reference current. Unfortunately, due to the distinctiveness the Vienna rectifier topology, severe zero-crossing current distortions may occur when the input voltage and the current are not in the same direction. Therefore, the conventional double-vector MPC method cannot be directly used for the Vienna rectifier. To overcome this limitation, Zhang et al. [18] proposed a double-vector MPC strategy without weighting factors for the Vienna rectifier with the goal of eliminating the current distortions, and some vectors are removed according to different sectors. However, when adjusting the NP voltage using P(positive)- or N(negative)-type small vectors, the switching frequency is forced to be unpredictable, leading to a complex task to design the filter. Besides, the two candidate vectors still limit the quality of the input current.

To achieve the fixed switching frequency (FSF), many MPC methods especially the finite-set MPC (FS-MPC) have been proposed. By setting the constraint of optimal pools such as the voltage vectors or switching sequences [19], [20], the FS-MPC can achieve the required control and the FSF is included. In [21], a two-stage MPC based on phase-shifted PWM (PS-PWM) is applied for a five-level active NP-clamped (5L-ANPC) converter. Using the interleaved carriers, the FSF can be conveniently realized. In [22], based on the capacitor voltages, the switching sequences are applied for a multilevel static synchronous compensator (STATCOM) to fix the switching frequency. For a seven-level hybrid multilevel converter (7L-HMC), a hybrid MPC method with independent low- and high-frequency stages is proposed in [23]. The optimized symmetric switching sequence can achieve the FSF. For three-level converters, Donoso et al. [24] propose an FS-MPC strategy for a neutral–point-clamping (NPC) converter with FSF using the nearest three vectors. Yang et al. [25] propose a virtual multiple voltage vector MPC strategy to split the sector into three subsectors for the T-type three-level converter. The virtual vector is synthesized by three vectors and it has no influence on the NP voltage. Notably, the above-mentioned two MPC strategies can be applied to common three-level rectifiers. However, in order to achieve decoupling of the FSF and current distortions, some vectors are abandoned [18] and the same candidate or virtual vectors cannot be utilized anymore for the Vienna rectifier. The NP voltage balancing strategy is also different when considering the FSF and current distortions together. In [24], the redundant small vectors (such as [PPO] and [OON]) are selected to balance the NP voltage. However, in Sector I in [15], the small vector [PPO] is removed to eliminate current distortions, which needs a new strategy to balance NP voltage and achieve the FSF. Besides, the removed vectors may lead the switching sequence to generate more switching transitions in one sampling period or between adjacent sampling periods. Therefore, it is urgent to achieve the FSF and NP voltage balance with less switching transitions for the Vienna rectifier.

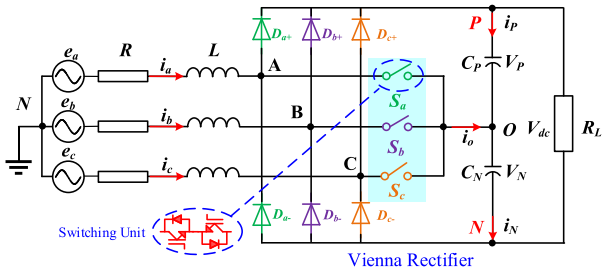

Fig. 1. Topology of Vienna rectifier.

In this article, an FSF-MPC method is proposed to fix the switching frequency per sampling period. Based on it, a FSF optimized (FSFO) MPC method is proposed to minimize the switching transitions between adjacent sampling periods to reduce the switching loss. To the best of authors' knowledge, so far, there exist a little FSF- and FSFO-MPC methods for the Vienna rectifier. The main contributions in this article are as follows.

1) The space vector diagram for the Vienna rectifier is divided into subsectors by two steps. Then they are recombined into novel N-or P-type regions to compensate for the absent vectors due to decoupling of the current distortion. In each new region, there are two sequences that can be used to balance the NP voltage. Simultaneously, each sequence can also achieve FSF per sampling period.
2) The sequence optimization between adjacent sampling periods is further considered. Based on the proposed FSF-MPC strategy, a novel sequence to save the switching transitions per sector between adjacent sampling periods is obtained. Compared with FSF-MPC strategy, the FSFO-MPC strategy can significantly reduce the switching loss and gain a high input current quality.
3) The results of the cost function after using in sector selection are reused to distribute the duty ratios of multiple vectors, which will not bring additional complex calculations. It can also increase the integrity and unity of the proposed MPC method for Vienna rectifier.

To demonstrate the proposed method in detail, this article is organized as follows. The mechanism for Vienna rectifier is introduced in Section II. FSF- and FSFO-MPC strategies are proposed in Section III. The effectiveness and feasibility of the two proposed methods are verified by the simulations and experiments in Section IV. Finally, the conclusions are given in Section V.

II. Description of Vienna Rectifier

The three-phase Vienna rectifier topology consists of three bidirectional switching units (S_a, S_b, and S_c) and six diodes as depicted in Fig. 1. The ac side of the Vienna rectifier is connected to the grid and the dc side is connected to the load. e_x $(x = a, b, c)$

TABLE I
SWITCHING STATES AND INPUT VOLTAGE OF VIENNA RECTIFIERS

Switching state	Condition	Switching function $S_x(x=a,b,c)$	u_{xo}
P	$i_x>0$	1	$V_{dc}/2$
O	$i_x>0$ / $i_x<0$	0	0
N	$i_x<0$	−1	$-V_{dc}/2$

TABLE II
RELATIONSHIP BETWEEN SWITCHING STATES AND VECTORS

Vectors	Names		
Zero	V_0 [OOO]		
Small	V_1 [POO]	V_2 [ONN]	V_3 [PPO]
	V_4 [OON]	V_5 [OPO]	V_6 [NON]
	V_7 [OPP]	V_8 [NOO]	V_9 [OOP]
	V_{10} [NNO]	V_{11} [POP]	V_{12} [ONO]
Medium	V_{19} [PON]	V_{20} [OPN]	V_{21} [NPO]
	V_{22} [NOP]	V_{23} [ONP]	V_{24} [PNO]
Large	V_{13} [PNN]	V_{14} [PPN]	V_{15} [NPN]
	V_{16} [NPP]	V_{17} [NNP]	V_{18} [PNP]

represents the line grid voltages. R and L denote the equivalent resistance and filter inductor, respectively. R_L is the dc-link load. In addition, the current flows into each phase is defined as ix ($x = a, b, c$) and the current flows out of the NP O is i_o. CP and CN are the upper and lower capacitors. V_P and V_N are the voltages of C_P and C_N, respectively. i_P and i_N are the currents flowing through C_P and C_N.

Due to the characteristics of the Vienna rectifier topology, it can be found that both switching function and the grid current direction have impact on the input voltage u_{xo} ($x = a, b, c$) as shown in Table I. It can be seen that the polarity of the input voltage and current is supposed to keep the same.

According to the length of the voltage vectors, they can be classified into four groups as listed in Table II. It can be observed that there is only one zero vector V_0[OOO] left, which is limited by the working principle of the Vienna rectifier.

From Fig. 1, the input voltage of the Vienna rectifier satisfies

$$u_{xo} = e_x - Ri_x - L\frac{di_x}{dt} x = (a, b, c) \tag{1}$$

where u_{xo} ($x = a, b, c$) is the three-phase input voltage.

Suppose that the NP voltage is balanced, according to Table I, the input voltage u_{xo} based on the switching function S_x can be expressed as follows:

$$u_{xo} = S_x \cdot \frac{V_{dc}}{2} (x = a, b, c). \tag{2}$$

Substituting (2) into (1), the input current can be calculated as follows:

$$Ri_x + L\frac{di_x}{dt} = e_x - S_x \cdot \frac{V_{dc}}{2} (x = a, b, c). \tag{3}$$

With the forward Euler approximation, the continuous model (3) can be rewritten in discrete form

$$i_x(k+1) = \frac{T_s}{M} \cdot e_x(k) + \frac{L}{M} i_x(k) - \frac{V_{dc} \cdot T_s}{2M} S_x(k) (x = a, b, c) \tag{4}$$

where $i_x(k)$ and $e_x(k)$ ($x = a, b, c$) are the three-phase input currents and the grid voltages at the kth instant, respectively. $S_x(k)$ is the switching function at the kth instant. $i_x(k+1)$ represent the predictive three-phase input currents at the $(k+1)$th instant. T_s is the sampling period. M is a constant value, which is defined as follows:

$$M = RT_s + L. \tag{5}$$

In Fig. 1, the upper and lower capacitors gain the same value C normally. Thus, the currents i_P, i_N, and i_o can be obtained as follows:

$$\begin{cases} i_P = C\frac{dV_P}{dt} = C\frac{d(V_{dc}-V_N)}{dt} = -i_N \\ i_o = i_N - i_P = 2i_N = -2i_P \end{cases}. \tag{6}$$

Using the Euler approximation to (6), the predictive voltage difference $\Delta V(k+1)$ between $V_P(k+1)$ and $V_N(k+1)$ at the $(k+1)$th instant is derived as follows:

$$\Delta V\,(k+1) = -\frac{i_o(k)}{C} T_s + \Delta V\,(k) \tag{7}$$

where $\Delta V(k)$ is the voltage difference between $V_P(k)$ and $V_N(k)$ at the kth instant.

According to Fig. 1, $i_o(k)$ is expressed as follows:

$$i_o(k) = (|S_x(k)| - 1) i_x(k) (x = a, b, c). \tag{8}$$

Substituting (8) into (7), $\Delta V(k+1)$ is calculated as follows:

$$\Delta V\,(k+1) = \frac{T_s}{C} (1 - |S_x(k)|) i_x(k) + \Delta V\,(k) \quad (x = a, b, c). \tag{9}$$

Assuming that the Vienna rectifier is operating under normal condition, two basic control targets including the input reference current tracking and NP voltage balancing are supposed to be achieved. Therefore, the conventional cost function is written as follows:

$$g_1(k) = \lambda_1 |i_x^*(k+1) - i_x(k+1)| + \lambda_2 |\Delta V\,(k+1)| \,(x = a, b, c) \tag{10}$$

where λ_1 is the weighting factor of the current tracking part, and λ_2 is the weighting factor of NP voltage balancing part. $i^*{}_x(k+1)$ ($x = a, b, c$) is the three-phase input reference current at the $(k+1)$th instant.

Based on the Lagrange extrapolation theorem, $i^*{}_x(k+1)$ is derived as follows:

$$i_x^*(k+1) = 3i_x^*(k) - 3i_x^*(k-1) + i_x^*(k-2) (x = a, b, c). \tag{11}$$

According to [18], for a rectifier, the reference input currents are derived as follows:

$$\begin{bmatrix} i_a^*(k) \\ i_b^*(k) \\ i_c^*(k) \end{bmatrix} = \frac{2}{3(e_\alpha^2(k) + e_\beta^2(k))} \begin{bmatrix} e_\alpha(k) & e_\beta(k) \\ e_\beta(k) & -e_\alpha(k) \end{bmatrix} \begin{bmatrix} P_{ref} \\ Q_{ref} \end{bmatrix} [\alpha\beta/abc] \tag{12}$$

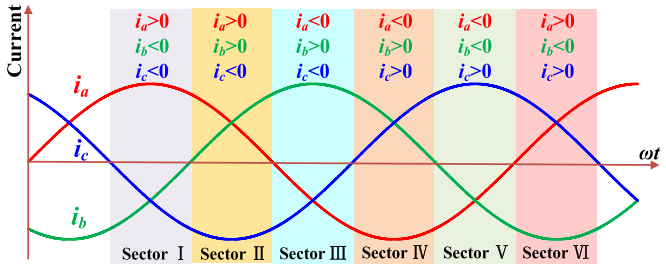

Fig. 2. Sector division based on the three-phase input currents.

where $e_\alpha(k)$ and $e_\beta(k)$ are the three-phase grid voltages in $\alpha\beta$-coordinate system at the kth instant. P_{ref} and Q_{ref} are the reference active power and the reference reactive power, respectively.

Although the cost function (10) can satisfy the two control targets, all the switching function $S_x(k)$s are required to iteratively be evaluated online according to (4) and (9). For the Vienna rectifier, there are total 25 space voltage vectors. Therefore, it is allowed to calculate 25 times per sampling period. More importantly, the selection and the adjustment of the weighting factors are a time-consuming progress.

For simplicity, the discrete model (4) based on voltage vectors in $\alpha\beta$-coordinate system is derived as follows:

$$\begin{bmatrix} u^*_\alpha(k) \\ u^*_\beta(k) \end{bmatrix} = \begin{bmatrix} e_\alpha(k) \\ e_\beta(k) \end{bmatrix} - \frac{M}{T_s}\begin{bmatrix} i^*_\alpha(k+1) \\ i^*_\beta(k+1) \end{bmatrix} + \frac{L}{T_s}\begin{bmatrix} i_\alpha(k) \\ i_\beta(k) \end{bmatrix} \tag{13}$$

where $u^*_\alpha(k)$ and $u^*_\beta(k)$ are the desired three-phase input voltages at kth instant in $\alpha\beta$-coordinate system.

Based on (13), the cost function (10) is rewritten as follows:

$$g_2(k) = \lambda_1(|u^*_\alpha(k) - u_\alpha(k)| + |u^*_\beta(k) - u_\beta(k)|) + \lambda_2 |\Delta V(k+1)| \tag{14}$$

where $u_\alpha(k)$ and $u_\beta(k)$ are the voltage vectors at the kth instant in the $\alpha\beta$-coordinate system.

Compared with (10), the redundant vectors are ignored and the number of the vectors is reduced from 25 to 19. However, (14) still includes weighting factors. Moreover, (14) is not considered to have FSF part. Therefore, it is highly required to realize the desired performance and simplify the MPC method, while achieving the two basic control targets in the cost function (14).

III. FSF- and FSFO-MPC Strategies

A. Sectors Division for Candidate Vectors

As previously analyzed, the input current and the phase voltage in the Vienna rectifier must be kept in the same direction to have a high power factor. Otherwise, serious input current distortion will occur.

To address the above-mentioned problem, the space voltage vector diagram can be divided into six sectors by the input current $i_x(k)$ in Fig. 2. For example, assuming that the $i_x(k)$ is located in Sector II, the sign of three-phase input currents is $[++-]$ at this time. As previously analyzed, the two redundant small voltage vectors [NON] and [OON] will produce serious current distortions. In other words, only eight space voltage

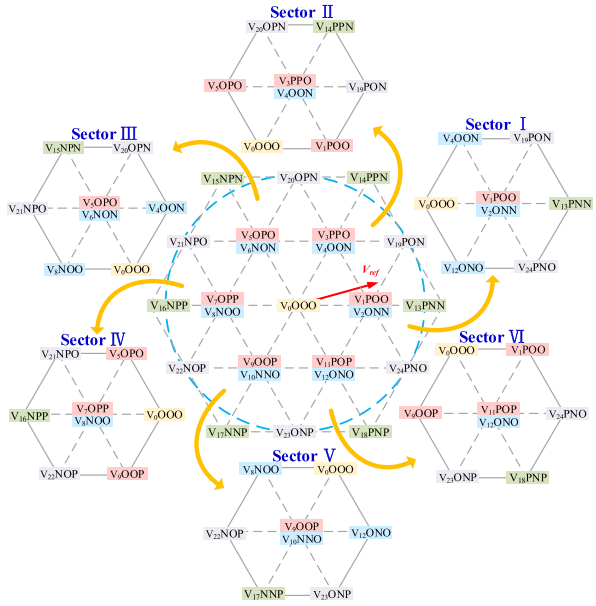

Fig. 3. Space voltage vector diagram from Sectors I to VI.

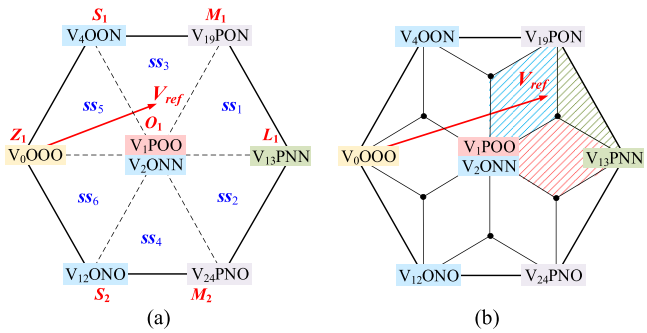

Fig. 4. Different ways of dividing Sector I. (a) Six subsectors divided with the proposed method. (b) Small areas divided with double-vector MPC.

vectors (V_0[OOO], V_1[POO], V_3[PPO], V_4[OON], V_5[OPO], V_{14}[PPN], V_{19}[PON], and V_{20}[OPN]) are selected as candidate vectors. Simultaneously, the number of candidate vectors will be reduced from 19 to 7 (including the two redundant small vectors).

Therefore, according to the different sectors, partial small voltage vectors which are not conformed to the above-mentioned principle are removed and six sectors are shown in Fig. 3.

Nevertheless, each sector can be further divided into six small subsectors (ss). Different from the conventional method, which relies on the amplitude and the phase angle of the reference voltage (V_{ref}) to determine subsectors, an FS-MPC strategy to divide the sectors based on cost function is proposed in this article.

Taking Sector I as an example in Fig. 4(a), it is supposed that (14) is only used to track the current at this time. The coordinates of the seven vectors are substituted into (14). Then, L_1, M_1, M_2, S_1, S_2, Z_1, and O_1 represent the calculated results of one large, two medium, two small, one zero, and one origin voltage vectors, respectively. The equation to select the ss_i is expressed

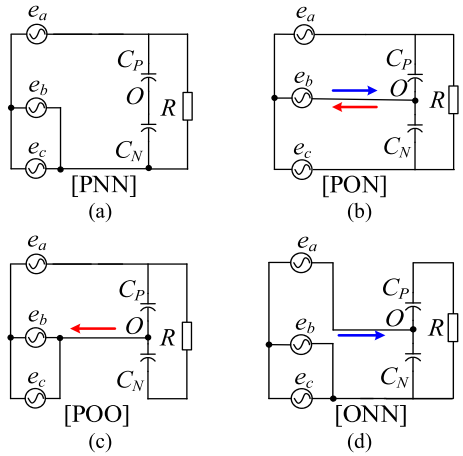

Fig. 5. Effect of partial vectors in Sector I on NP voltage. (a) [PNN]. (b) [PON]. (c) [POO]. (d) [ONN].

as follows:

$$\begin{aligned} ss_i &= \min\{p_i\}, i \in \{1,2,3,4,5,6\} \\ p_1 &= L_1 + M_1, p_2 = L_1 + M_2, p_3 = M_1 + S_1 \\ p_4 &= M_2 + S_2, p_5 = S_1 + Z_1, p_6 = S_1 + Z_2. \end{aligned} \tag{15}$$

For example, if p_3 is the minimum of p_i ($i = 1, 2 \cdots 6$), V_{ref} is located in ss_3 as shown in Fig. 4(a). The other five sectors which can be obtained from Sector I rotating around V_0[OOO] also follow the same principle.

B. Balancing the NP Voltage and Fixing the Switching Frequency

For the conventional method, the effective way to control the NP voltage is to use different types of vectors as shown in Fig. 5 [26]. Taking Sector I as an example, the large vector [PNN] in Fig. 5(a) cannot affect the NP voltage whereas the medium vector [PON] in Fig. 5(b) leads to an imbalance of the NP voltage. The small P-type vector [POO] can discharge the upper capacitor C_P and charge the lower capacitor C_N as shown in Fig. 5(c). On the contrary, the small N-type vector [ONN] can discharge the lower capacitor C_N and charge the upper capacitor C_P in Fig. 5(d).

Therefore, with the double-vector MPC method in [18], the NP voltage is balanced by selecting P- or N-type small vectors. However, the switching frequency is not fixed in this way. Assuming the V_{ref} is located in ss_1 as depicted in Fig. 4(b), it can be observed that ss_1 can be further divided into three small shadow areas. In the blue shadow area, the candidate two-segment sequences are [PON]-[POO] and [PON]-[ONN], respectively. In the red shadow area, the candidate two-segment sequences are [PNN]-[POO] and [PNN]-[ONN], respectively. In the green shadow area, the only one two-segment sequence is [PON]-[PNN]. Obviously, except the green shadow area, the switching frequency in the other two areas is affected by the fluctuation of the NP voltage.

All in all, it is apparently impossible to achieve the FSF only by switching N- or P-type small vectors and highly desirable to propose a strategy to achieve both NP voltage balancing and the FSF.

TABLE III
SIX SEVEN-SEGMENT SEQUENCES IN SECTOR I

Subsector	Seven-segment sequence
ss_1	[ONN]-[PNN]-[PON]-[POO]-[PON]-[PNN]-[ONN]
ss_2	[ONN]-[PNN]-[PNO]-[POO]-[PNO]-[PNN]-[ONN]
ss_3	[ONN]-[OON]-[PON]-[POO]-[PON]-[OON]-[ONN]
ss_4	[ONN]-[ONO]-[PNO]-[POO]-[PNO]-[ONO]-[ONN]
ss_5	[ONN]-[OON]-[OOO]-[POO]-[OOO]-[OON]-[ONN]
ss_6	[ONN]-[ONO]-[OOO]-[POO]-[OOO]-[ONO]-[ONN]

With the conventional modulation method of the three-level converters, the nearest four candidate vectors are selected to generate a seven-segment waveform. Among these four candidate vectors, usually two small vectors are N-type and P-type, respectively. Therefore, as long as the sum of the duty ratio of the two redundant small vectors remains constant, the NP voltage is balanced by adjusting the dwell times of N- and P-type small vectors. In addition, using the above-mentioned conventional modulation strategy, the FSF is also achieved simultaneously.

As for the Vienna rectifier, taking Sector I as an example, the six seven-segment sequences in ss_1 to ss_6 are listed in Table III.

It can be seen in Table III that the above-mentioned seven-segment sequences can achieve the FSF. However, except the sequences in ss_1 and ss_2, the absence of P-type small vectors leads to the negative polarity (negative polarity in odd sectors while positive polarity in even sectors) of the rest four sequences. Although the dwell time of the redundant N-type vector [ONN] can be set to zero to alleviate the negative polarity, the new five-segment sequence reduces the ability of balancing the NP voltage. For example, after removing the N-type vector [ONN] in the sequence of ss_3 in Table III, the new five-segment sequence is becoming [OON]-[PON]-[POO]-[PON]-[OON]. Based on the symmetry of the sectors, the average current flowing out of the NP is zero, which will not bring the NP voltage imbalance. However, it cannot recover the NP voltage either when the imbalance occurs. Thus, it can be concluded that the current zero-crossing distortion, the FSF, and the NP voltage balancing are coupled.

In fact, as long as each region contains both N-type and P-type sequences, the NP voltage can be balanced. Inspired by the previous analysis, the sector is supposed to be classified according to its parity.

Take Sectors I and II as an example. In Sector I, since the P-type vectors [PPO] and [POP] are removed as shown in Fig. 3, all the sequences in six subsectors are required to contain the left P-type vector [POO] and no N-type vectors to ensure that the sequences tend to be P-type. Therefore, ss_3 and ss_5 are combined into one region P_{III} as shown in Fig. 6(a). Similarly, P_{IV} can also be derived from ss_4 and ss_6 in Fig. 6(a). The P-type sequences in P_{III} and P_{IV} are [OOO]-[POO]-[PON]-[POO]-[OOO] and [OOO]-[POO]-[PNO]-[POO]-[OOO], respectively. As for P_I and P_{II}, the P-type sequences are designed as [POO]-[PON]-[PNN]-[PON]-[POO] and [POO]-[PNO]-[PNN]-[PNO]-[POO]. Therefore, based on

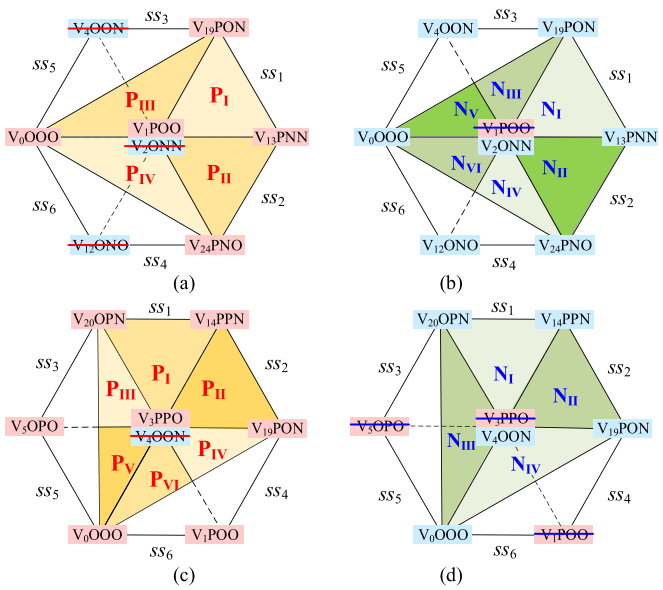

Fig. 6. Different ways of dividing Sectors I and II. (a) Four P-type regions in Sector I. (b) Six N-type regions in Sector I. (c) Six P-type regions in Sector II. (d) Four N-type regions in Sector II.

the above-mentioned method of dividing the sector into four P-type regions, Sector I can be positive. The P-type sequences in P_I and P_{III} of Sector I are illustrated in Fig. 7(a) and (b), respectively.

Unlike the P-type small vectors, the N-type small vector is not removed in Sector I. Thus, the subsector does not need to be merged like the P-type condition described earlier, and Sector I is still divided into six negative regions in Fig. 6(b) (N_I, N_{II}, N_{III}, N_{IV}, N_V, and N_{VI}). In contrary to the P-type sequence, each N-type sequence contains at least one N-type small vector, which makes the entire sequence negative. Therefore, Sector I can also be negative. The N-type sequences in N_I, N_{III}, and N_V of Sector in Ntire sequence negFig. 7(c), (d), and (e), respectively.

As for Sector II, contrary to Sector I, the N-type vectors are removed as shown in Fig. 3. Therefore, the method to divide Sector II into N-type regions is the same as that of dividing Sector I into P-type regions as shown in Fig. 6(d). Sector II can be also divided into six P-type regions as shown in Fig. 6(c). Consequently, Sector II contains both N- and P-type five-segment sequences. In Sector II, the P-type sequences in P_I, P_{III}, and P_V and the N-type sequences in N_I, N_{III} are illustrated in Fig. 7(f)–(j) in turns.

According to the parity of the other four sectors, the odd sectors (Sectors III and V) follow the dividing principle of Sector I and the even sectors (Sectors IV and VI) follow Sector II.

Thus, each sector contains N-type and P-type switching sequences determined by the fluctuation of NP voltage. Due to no redundant vectors, the three candidate vectors will generate a five-segment sequence. In each sampling period, one of the three phases is always clamped to keep the switching state unchanged, and the other two-phase switches only act once, which achieves the FSF.

Consequently, the weighting factor λ_2 to balance the NP voltage is removed in (14) and the new cost function consisting of only one term to penalize the error between the reference voltage and the predictive voltage is derived as follows:

$$g_3(k) = |u_\alpha^*(k+1) - u_\alpha(k+1)| + |u_\beta^*(k+1) - u_\beta(k+1)|. \tag{16}$$

According to Fig. 3, after dividing the sector, the candidate vectors are reduced from 19 to 7, which further lessens the computational burden.

TABLE IV
FIVE-SEGMENT SEQUENCES IN SECTOR I

Subsector		Five-segment sequence
ss_1	N_I	[PON]-[PNN]-[ONN]-[PNN]-[PON]
	P_I	[PNN]-[PON]-[POO]-[PON]-[PNN]
ss_2	N_{II}	[PNO]-[PNN]-[ONN]-[PNN]-[PNO]
	P_{II}	[PNN]-[PNO]-[POO]-[PNO]-[PNN]
ss_3	N_{III}	[PON]-[OON]-[ONN]-[OON]-[PON]
	P_{III}	[PON]-[POO]-[OOO]-[POO]-[PON]
ss_4	N_{IV}	[PNO]-[ONO]-[ONN]-[ONO]-[PNO]
	P_{IV}	[PNO]-[POO]-[OOO]-[POO]-[PNO]
ss_5	N_V	[OOO]-[OON]-[ONN]-[OON]-[OOO]
	P_{III}	[OOO]-[POO]-[PON]-[POO]-[OOO]
ss_6	N_{VI}	[OOO]-[ONO]-[ONN]-[ONO]-[OOO]
	P_{IV}	[OOO]-[POO]-[PNO]-[POO]-[OOO]

C. Optimizing Switching Sequence Between the Adjacent Sampling Period

In order to reduce the switching loss between the adjacent sampling periods, the switching sequence needs to be further optimized.

Take Sector I as an example. In ss_1 (ss_2), the shape of P_I (P_{II}) in Fig. 6(a) is the same as that of N_I (N_{II}) in Fig. 6(b). Therefore, the P-type and N-type five-segment sequences are, respectively, designed as [PNN]-[PON]-[POO]-[PON]-[PNN] and [PON]-[PNN]-[ONN]-[PNN]-[PON] ([PNN]-[PNO]-[POO]-[PNO]-[PNN] and [PNO]-[PNN]-[ONN]-[PNN]-[PNO]). It is observed that when the sequence needs to switch in the next sampling period, the direct transition between state P and N is avoided and only one-phase switch is operated.

In ss_3 and ss_5, there are two kinds of P-type sequences in P_{III}, which are listed as [PON]-[POO]-[OOO]-[POO]-[PON] and [OOO]-[POO]-[PON]-[POO]-[OOO], respectively. In order to minimize the switching transitions between the adjacent sampling periods when balancing the NP voltage, one effective method is to keep the last vector of the previous switching sequence and the first vector of the next switching sequence the same. Therefore, the N-type sequence in N_{III} (also in ss_3) is designed as [PON]-[OON]-[ONN]-[OON]-[PON]. Similarly, the sequence in N_V (also in ss_5) is designed as [OOO]-[OON]-[ONN]-[OON]-[OOO]. Compared with the P-type sequences in ss_3 or ss_5, the switching transitions between the adjacent sampling periods are saved apparently. The same designed principle is also suitable for ss_4 and ss_6. All the five-segment sequences in Sector I are summarized in Table IV.

As for the even sectors such as Sector II, the analysis of ss_1 and ss_2 is the same as that of Sector I. Reversing the N-type regions and P-type regions can simply obtain the switching sequence of

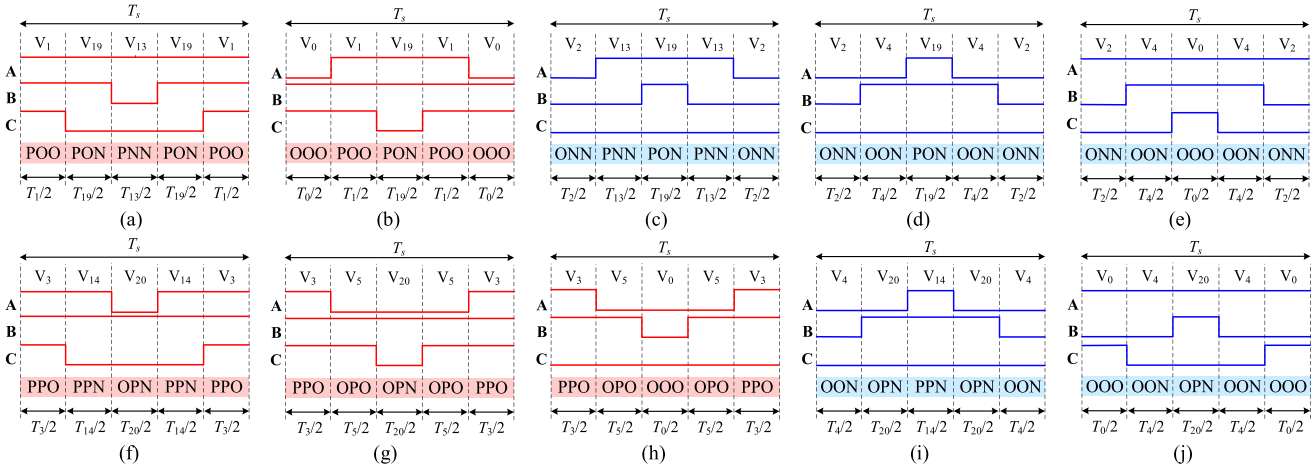

Fig. 7. Partial five-segment sequences in Sectors I and II. (a) P_I of Sector I. (b) P_{III} of Sector I. (c) N_I of Sector I. (d) N_{III} of Sector I. (e) N_V of Sector I. (f) P_I of Sector II. (g) P_{III} of Sector II. (h) P_V of Sector II. (i) N_I of Sector II. (j) N_{III} of Sector II.

TABLE V
FIVE-SEGMENT SEQUENCES IN SECTOR II

Subsector		Five-segment sequence
ss_1	N_I	[PPN]-[OPN]-[OON]-[OPN]-[PPN]
	P_I	[PPO]-[PPN]-[OPN]-[PPN]-[PPO]
ss_2	N_{II}	[PPN]-[PON]-[OON]-[PON]-[PPN]
	P_{II}	[PPO]-[PPN]-[PON]-[PPN]-[PPO]
ss_3	N_{III}	[OPN]-[OON]-[OOO]-[OON]-[OPN]
	P_{III}	[OPN]-[OPO]-[PPO]-[OPO]-[OPN]
ss_4	N_{IV}	[PON]-[OON]-[OOO]-[OON]-[PON]
	P_{IV}	[PON]-[POO]-[PPO]-[POO]-[PON]
ss_5	N_{III}	[OOO]-[OON]-[OPN]-[OON]-[OOO]
	P_V	[OOO]-[OPO]-[PPO]-[OPO]-[OOO]
ss_6	N_{IV}	[OOO]-[OON]-[PON]-[OON]-[OOO]
	P_{VI}	[OOO]-[POO]-[PPO]-[POO]-[OOO]

the rest four subsectors (ss_3, ss_4, ss_5, and ss_6). The five-segment sequences of Sector II are listed in Table V.

Besides achieving the FSF, the FSFO-MPC can effectively reduce the switching loss between adjacent sampling periods.

D. Duty Ratios Calculation

The conventional SVPWM adopts the nearest three voltage vectors with the volt-second balance to synthesize V_{ref}. The restriction formula is expressed as follows:

$$\begin{cases} d_{c1}V_{c1} + d_{c2}V_{c2} + d_{c3}V_{c3} = V_{ref} \\ d_{c1} + d_{c2} + d_{c3} = 1 \end{cases} \tag{17}$$

where d_{c1}, d_{c2}, and d_{c3} represent the duty ratio of the three candidate vectors V_{c1}, V_{c2}, and V_{c3}, respectively.

It is observed that (16) calculates the distance from V_{ref} to seven fixed vectors in each sector, which means that the larger result of cost function is, the farther voltage vector is from V_{ref}. Thus, the duty ratio is inversely proportional to the result of the cost function, which is expressed as follows:

$$d_{cy} = \frac{K}{g_{cy}} \quad (y = 1, 2, 3) \tag{18}$$

where K is the scale factor and $K \geq 0$. g_{cy} is the result of (16) corresponding to the candidate three voltage vectors V_{c1}, V_{c2}, and V_{c3}.

Substituting (17) into (18), the scale factor K is calculated as follows:

$$K = \frac{g_{c1}g_{c2}g_{c3}}{g_{c1}g_{c2} + g_{c2}g_{c3} + g_{c1}g_{c3}}. \tag{19}$$

Since the results of the cost function are all non-negative, the scale factor K can be guaranteed to be greater than or equal to 0. Therefore, the calculated duty ratios are also non-negative and they can be expressed as follows:

$$\begin{cases} d_{c1} = \frac{g_{c2}g_{c3}}{g_{c1}g_{c2}+g_{c2}g_{c3}+g_{c1}g_{c3}} \\ d_{c2} = \frac{g_{c1}g_{c3}}{g_{c1}g_{c2}+g_{c2}g_{c3}+g_{c1}g_{c3}} \\ d_{c3} = \frac{g_{c1}g_{c2}}{g_{c1}g_{c2}+g_{c2}g_{c3}+g_{c1}g_{c3}} \end{cases}. \tag{20}$$

With the duty ratios of the three candidate vectors, a five-segment sequence will be generated.

As previously analyzed, the existing MPC methods for Vienna rectifier cannot address these issues of controlling multiple targets such as the current distortion elimination, the current ripples reduction, NP voltage balance, and fixing the switching frequency. To address the above-mentioned issue, the FSF- and FSFO-MPC strategies are proposed and the flow chart with five steps of the two methods for Vienna rectifier is illustrated in Fig. 8.

IV. SIMULATION AND EXPERIMENTAL RESULTS

A. Simulation Results

To prove the effectiveness and feasibility of the proposed method, the Vienna rectifier system is simulated in MATLAB/Simulink. The parameters of the simulations are shown in Table VI. There are four different MPC methods as listed in Table VII. Among these, FSF- and FSFO-MPC methods are the novel methods proposed in this article.

Figs. 9 and 10 are the steady-state simulation waveforms of three-phase line-to-line voltages and input currents of four

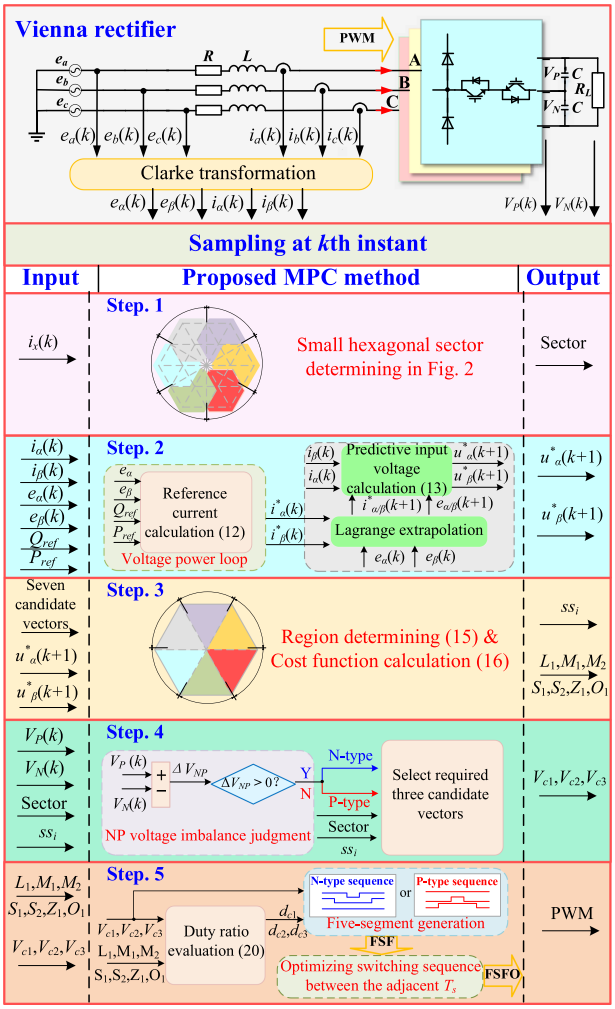

Fig. 8. Flow chart of the proposed MPC method.

TABLE VI
PARAMETERS FOR SIMULATIONS AND EXPERIMENTS

Grid voltage (e_a, e_b, e_c)	150 V [peak]
Dc-link voltage (V_{dc})	400 V
Dc-link capacitor (C)	1000 μF
Dc-link Load (R_L)	65 Ω / 100 Ω
Equivalent resistance (R)	0.1 Ω
L-filter (L)	5 mH
Switching frequency (f_s)	10 kHz
Sampling time (T_s)	100 μs

TABLE VII
FOUR DIFFERENT CONTROL METHODS

MPC-1	Conventional MPC method with all vectors
MPC-2	Double-vector MPC method [18]
MPC-3	Proposed FSF-MPC method
MPC-4	Proposed FSFO-MPC method

TABLE VIII
SIMULATED THDS OF FOUR METHODS UNDER VARIOUS R_LS

Method	THD (R_L=65 Ω)	THD (R_L=100 Ω)
MPC-1	17.89%	6.99%
MPC-2	4.34%	6.04%
MPC-3	3.43%	4.68%
MPC-4	3.50%	4.70%

methods listed in Table VII with 400 V on the dc-side. The eight corresponding total harmonic distortions (THDs) are listed in Table VIII.

As analyzed in Section II, only keeping the voltage and current in the same direction can the Vienna rectifier operate normally. Therefore, when using MPC-1, all the vectors including those causing the current distortion are selected as candidate vectors, resulting in serious distortion of the input current as shown in Fig. 9(a) and the THD of the input current is as high as 17.89%. Similarly, the zoom-in view of the line-to-line voltage in Fig. 9(a) exists some undesired voltage steps when crossing the zero-axis. This is because the phase voltage of MPC-1 is formed by the wrong voltage vectors and the Vienna rectifier cannot generate the corresponding phase voltage in this condition. In Fig. 10(a), with the increasing of R_L from 65 to 100 Ω, the amplitude of the input current is reduced to 8 A. Still, from its zoom-in view the current distortion exists at the zero crossing point and the THD is 6.99%. It is worth noting that the conventional MPC method MPC-1 can be applied to the three-level T-type rectifier, etc. However, it cannot be used for Vienna rectifier topology directly.

It is seen in Figs. 9(b) and 10(b) that the input current zero-crossing distortion has disappeared whereas there is another distortion at the current peak with MPC-2. The THDs with two different R_Ls are 4.32% and 6.04%, respectively. In addition, the line-to-line voltage waveform presents a ladder shape and it is similar to that of adopting SVPWM. This is due to the fact that the V_{ref} is synthesized by two nearest vectors which are certainly any two of the three vectors from the NTVSVPWM (nearest-three vectors SVPWM) method. Among the nearest-three vectors (excluding redundant ones), the double-vector selection options are totally ${C_3}^2 = 3$. Therefore, the uncertainty of the above-mentioned options causes the non-FSF.

When MPC-3 and MPC-4 are adopted, the waveforms of their currents and line-to-line voltage are basically the same as depicted in Fig. 9(c) and (d). The current waveform is sinusoidal without distortions. Besides, between −200 V to 0 V and 0 V to 200 V, there exists a line-to-line voltage jump, indicating that at this moment the candidate vectors are located in the area like P_{III} as shown in Fig. 6(a).

Other zoom-in views of MPC-2, MPC-3, and MPC-4 in Figs. 9 and 10 show no distortion of the line-to-line voltage and the three-phase current can cross the zero-axis smoothly, which indicates the candidate vectors in Fig. 3 are correct.

The fast Fourier transform (FFT) diagrams of MPC-3 and MPC-4 corresponding to Fig. 9(c) and (d) and Fig. 10(c) and (d) are illustrated in Fig. 11. Since both methods adopt FSF,

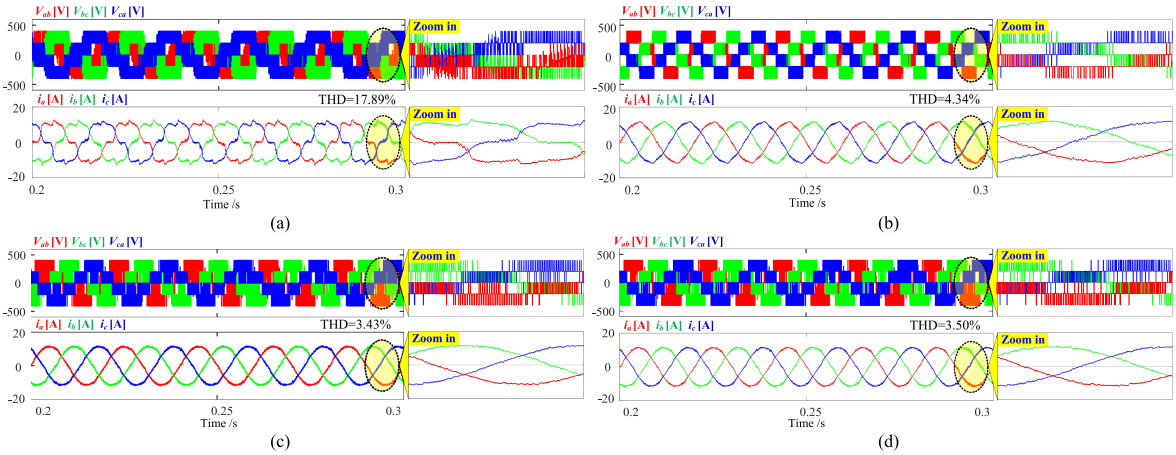

Fig. 9. Simulation waveforms of line-to-line voltages and input currents with different methods under $R_L = 65\ \Omega$. (a) MPC-1. (b) MPC-2. (c) MPC-3. (d) MPC-4.

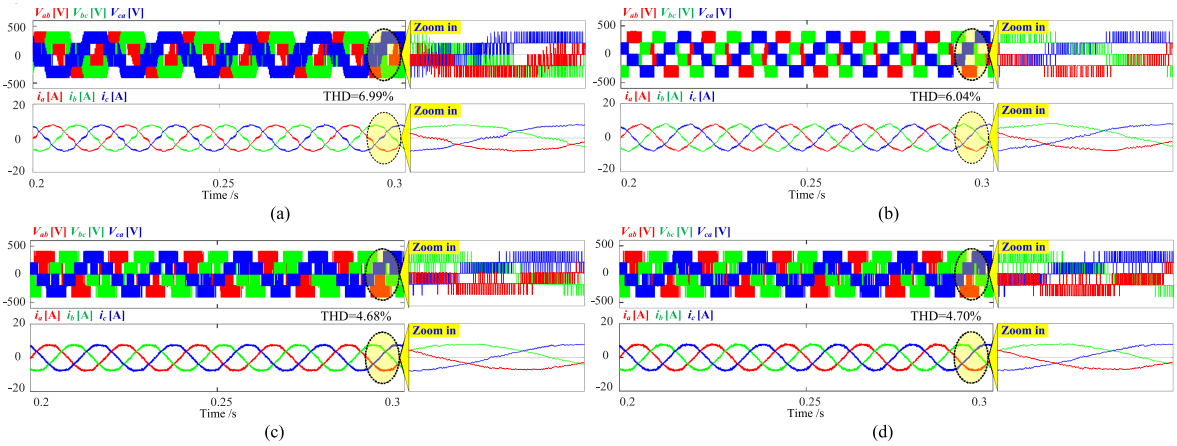

Fig. 10. Simulation waveforms of line-to-line voltages and input currents with different methods under $R_L = 100\ \Omega$. (a) MPC-1. (b) MPC-2. (c) MPC-3. (d) MPC-4.

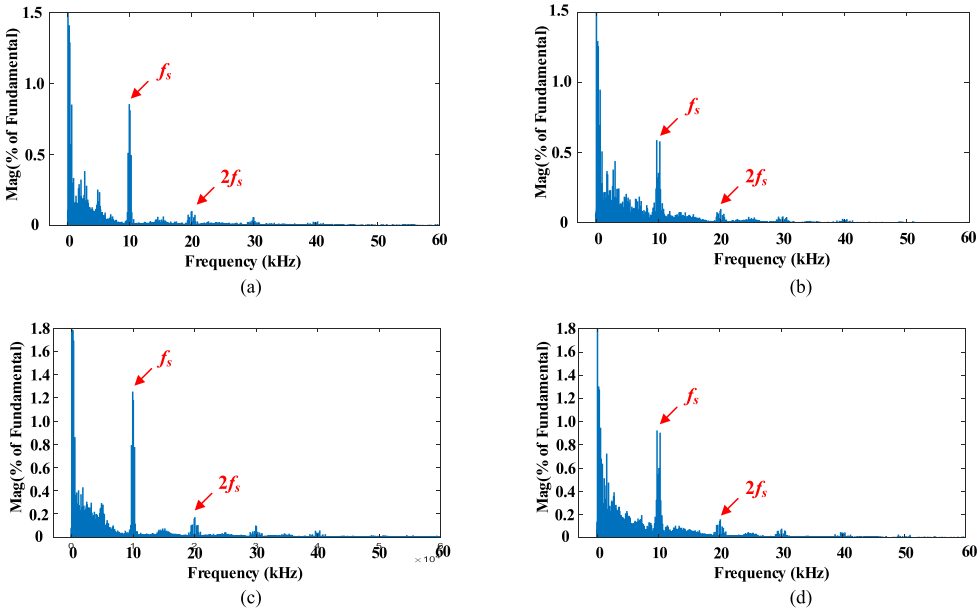

Fig. 11. Simulation FFT diagrams of MPC-3 and MPC-4 under different R_L. (a) MPC-3 with $R_L = 65\ \Omega$. (b) MPC-4 with $R_L = 65\ \Omega$. (c) MPC-3 with $R_L = 100\ \Omega$. (d) MPC-4 with $R_L = 100\ \Omega$.

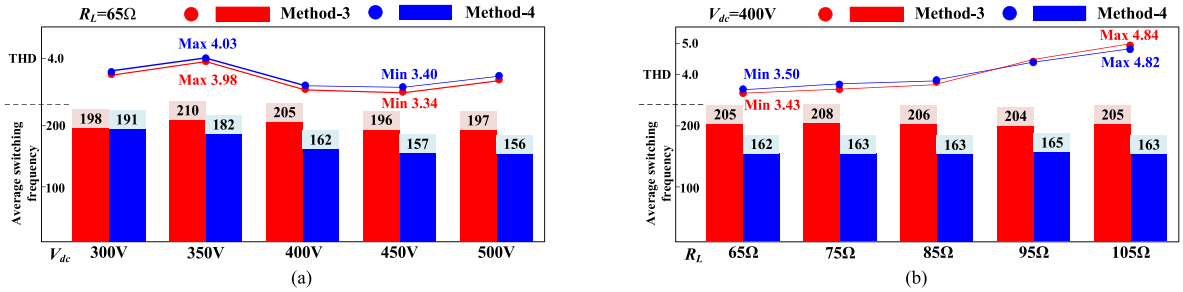

Fig. 12. Effects on THDs and the average switching frequency under different variables with MPC-3 and MPC-4. (a) Different V_{dc} and $R_L = 65\ \Omega$. (b) Different R_L and $V_{dc} = 400$ V.

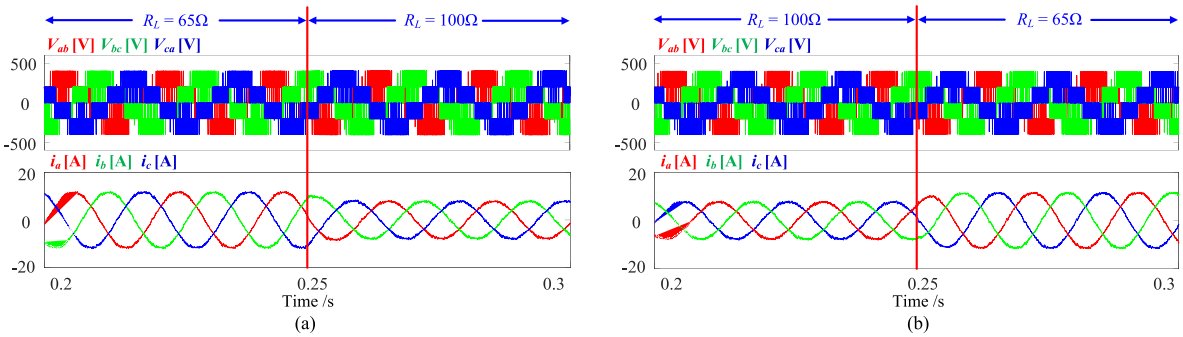

Fig. 13. Dynamic simulation waveforms of line-to-line voltage V_{ab} and input current i_{abc} with MPC-4 method. (a) R_L from 65 Ω to 100 Ω. (b) R_L from 100 Ω to 65 Ω.

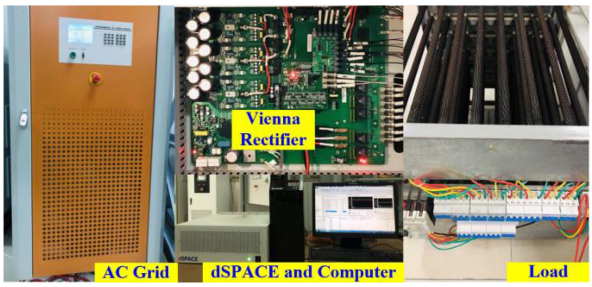

Fig. 14. Experimental platform of Vienna rectifier control.

the frequency is mostly concentrated in the integer multiple of the f_s (10 kHz), such as $2f_s$ (20 kHz). It can be observed that in Fig. 11(b) and (d), there is a sideband harmonic around f_s caused by the discontinuous clamping and the reorder of five-segment sequence, which is consistent with the DPWM method [27].

As introduced before, MPC-4 optimizes the sequence switching between adjacent sampling periods when balancing the NP voltage. Hence, it can effectively reduce the switching loss compared with MPC-3. In this article, three variables have impacts on the switching loss: method, R_L, and V_{dc}. Therefore, the control variable method is adopted to compare the average switching frequency and the THD values of MPC-3 and MPC-4 under different V_{dc} and R_L, respectively.

According to [17], the average switching frequency of the Vienna rectifier can be expressed as follows:

$$f_w = \frac{f_a}{6N} \sum_{i=0}^{N-1} S_w(i) \tag{21}$$

where $N = f_a/f$. f_a is the sampling frequency ($1/T_s$); f is the fundamental frequency (50 Hz); $S_w(i)$ is the switching frequency in one sampling period; and 6 means the number of all power switches of Vienna rectifier. The results are summarized in Fig. 12.

It is observed in Fig. 12(a) that when the V_{dc} is small, the average switching frequency of MPC-3 and MPC-4 is basically the same. Since the modulation index is large, V_{ref} is mostly located in ss_1 and ss_2. According to Tables IV and V, in the above-mentioned subsectors, the switching transition between P- and N-type sequences is avoided for both two MPC methods. When the V_{dc} gradually increases, the corresponding modulation index is getting smaller, and V_{ref} is mostly located in ss_3, ss_4, ss_5, and ss_6. According to Tables IV and V, the switching transitions of MPC-4 in adjacent sampling period are effectively avoided per sector whereas MPC-3 only designs the five-segment sequence in each sampling period. Thus, the average switching frequency of MPC-3 is higher than MPC-4. When the load R_L gradually increases as shown in Fig. 12(b), since the V_{dc} and the grid voltage keep constant, the subsectors which V_{ref} passes are basically the same. Therefore, the average switching frequency of two MPC methods is almost constant.

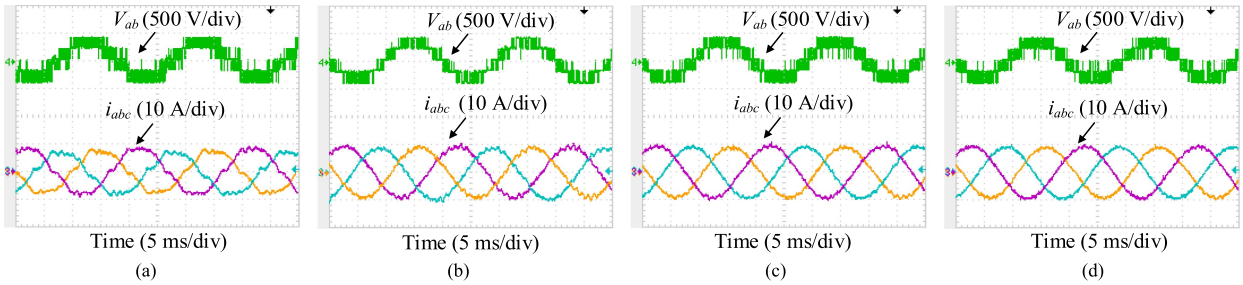

Fig. 15. Steady-state experimental waveforms under $R_L = 65\ \Omega$ of the line-to-line voltage and the input currents. (a) MPC-1. (b) MPC-2. (c) MPC-3. (d) MPC-4.

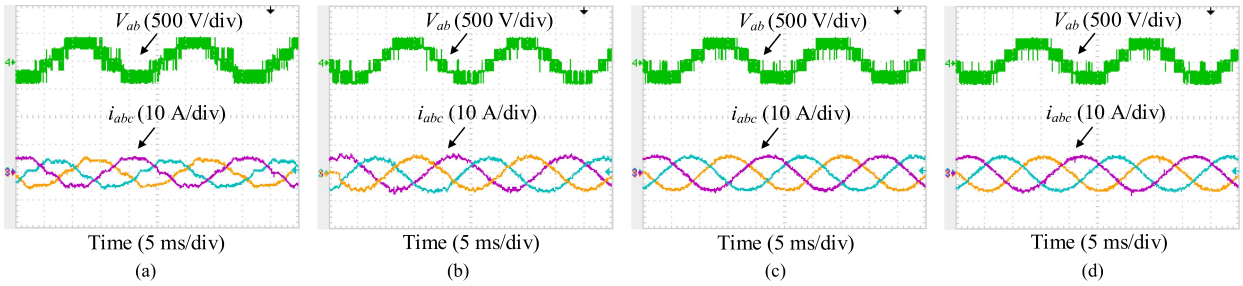

Fig. 16. Steady-state experimental waveforms under $R_L = 100\ \Omega$ of the line-to-line voltage and the input currents. (a) MPC-1. (b) MPC-2. (c) MPC-3. (d) MPC-4.

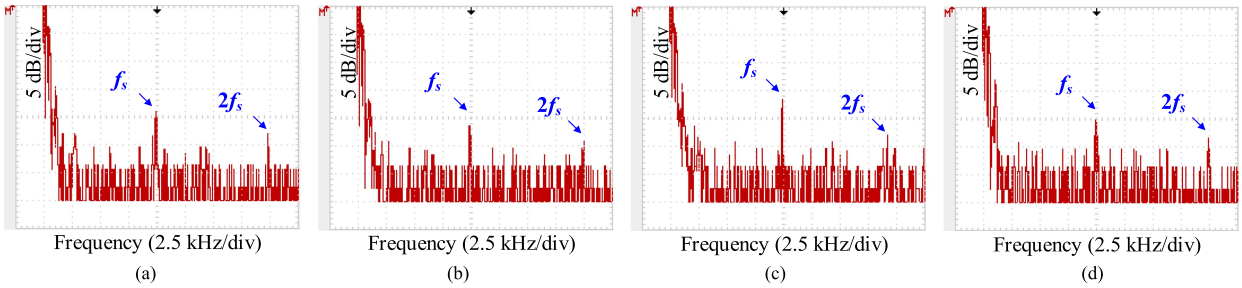

Fig. 17. Experimental FFT diagrams impact of current of MPC-3 and MPC-4 under different R_Ls. (a) MPC-3 with $R_L = 65\ \Omega$. (b) MPC-4 with $R_L = 65\ \Omega$. (c) MPC-3 with $R_L = 100\ \Omega$. (d) MPC-4 with $R_L = 100\ \Omega$.

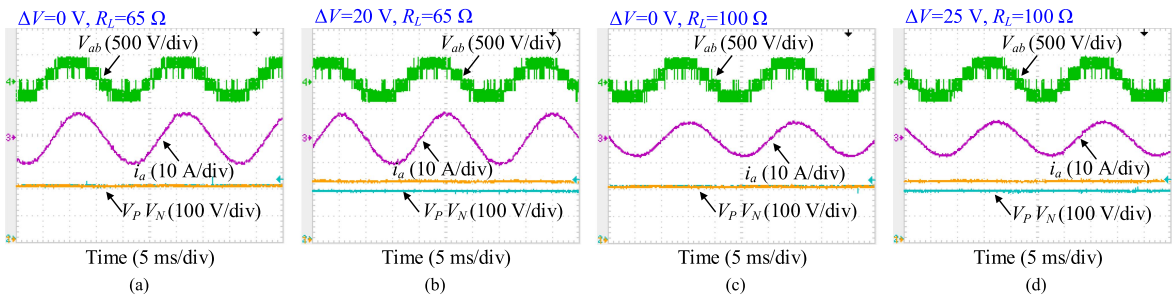

Fig. 18. Steady-state experimental waveforms of and line-to-line voltage V_{ab}, input current i_a, V_P, and V_N with MPC-4. (a) $R_L = 65\ \Omega$, $\Delta V_{PN} = 0$ V. (b) $R_L = 65\ \Omega$, $\Delta V_{PN} = 20$ V. (c) $R_L = 100\ \Omega$, $\Delta V_{PN} = 0$ V. (d) $R_L = 100\ \Omega$, $\Delta V_{PN} = 20$ V.

However, due to the reordering of candidate sequences as listed in Tables IV and V, the average switching frequency of MPC-4 is lower than that of MPC-3. Besides, it is observed that the THD values of MPC-3 and MPC-4 in Fig. 12 are almost the same, which indicates that the reordering of the sequence will not affect the quality of the input current greatly.

All in all, whether changing V_{dc} or R_L, the average switching frequency of MPC-4 is smaller than that of MPC-3, demonstrating the FSFO-MPC strategy can reduce the switching loss compared with the FSF-MPC strategy.

The condition of a load step on R_L is shown in Fig. 13. It can be seen whether R_L becomes larger or smaller, the amplitude

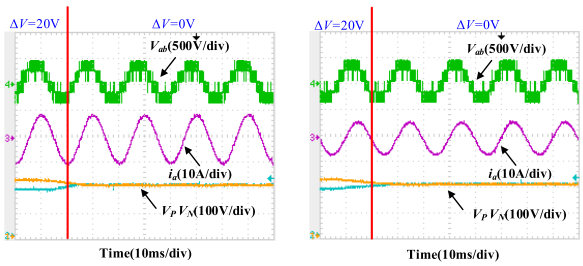

Fig. 19. Dynamic experimental waveforms of line-to-line voltage V_{ab}, input current i_a, V_P, and V_N with MPC-4 method. (a) $R_L = 65\ \Omega$. (b) $R_L = 100\ \Omega$.

of input currents can quickly catch up with the R_L change, indicating that MPC-4 method gains a fast dynamic response.

B. Experimental Results

To further verify the validity of the proposed FSF- and FSFO-MPC strategies, a series of experiments have been carried out with a Vienna rectifier as shown in Fig. 14. dSPACE is the main controller of the whole system. The experimental parameters are listed in Table VI.

Like the simulation, the experiment is also conducted using the four MPC methods as shown in Table VII.

When $R_L = 65\ \Omega$, due to using all vectors with MPC-1, serious input current distortions occur as shown in Fig. 15(a). Although MPC-2 in Fig. 15(b) removes those vectors causing the current distortions, fewer vectors for synthesis will lead to poor quality input currents. Moreover, the switching frequency is not fixed, which improves the difficulty of designing the filters. The input currents with MPC-3 and MPC-4 are much smoother in Fig. 15(c) and (d). The line-to-line voltages exist in the jump from 0 V to 200 V or −200 V to 0 V, which is caused by the composite P-type or N-type regions like P_{III} in Sector I or N_{III} in Sector II.

When $R_L = 100\ \Omega$, the amplitude of the input current decreases accordingly. The current distortions still exist with MPC-1 in Fig. 16(a). The input current quality of MPC-2 is worse as shown in Fig. 16(b), indicating the double-MPC method is greatly affected by different R_Ls. Although those current harmonics can be reduced by larger inductance, it will increase the volume of the inductance. Compared with MPC-1 and MPC-2, the input current quality of MPC-3 and MPC-4 is still high as shown in Fig. 16(c) and (d). This is because the above-mentioned two methods adopt multiple vectors. As shown in Fig. 17, like the simulation results in Fig. 11, the high-order harmonics are also concentrated at the integer multiple of f_s, such as $2f_s$ (20 kHz), indicating both two methods can achieve the FSF

The steady-state experimental waveforms of MPC-4 are shown in Fig. 18. Due to the fact that each subsector contains both N- and P-type sequences, the ΔV can be controlled at any difference and $\Delta V = 0$ V is the special case. Specifically, when $R_L = 65\ \Omega$, the steady-state waveforms in the case of $\Delta V = 0$ V and $\Delta V = 20$ V are illustrated in Fig. 11(a) and (b), respectively. When R_L is changed to 100 Ω, the above-mentioned two cases are depicted in Fig. 11(c) and (d).

The dynamic experiment as shown in Fig. 19 is conducted for further verifying the control performance of the proposed MPC-4 method. To demonstrate the ability of the control of NP voltage under two R_L, the ΔV is set as 20 V at first in Fig. 19. When the NP balance strategy is adopted, the ΔV is reduced quickly from 20 V to 0 V under $R_L = 65\ \Omega$. Similarly, when $R_L = 100\ \Omega$, the NP voltage can be still recovered. Therefore, by switching P- and N-type sequences, the NP voltage can recover immediately when the imbalance on dc side occurs.

V. Conclusion

The Vienna rectifier faces many challenges such as FSF, current distortion elimination, current ripple reduction, switching loss reduction, and NP voltage balance. For the sake of the coupling of the above-mentioned issues, the mentioned problem cannot be solved with the conventional methods properly. Thus, two novel FSF- and FSFO-MPC methods are proposed. By the effective performance conducted in simulation and experiment, the conclusions can be summarized as follows.

1) The decoupling is realized, and the NP voltage is balanced while also eliminating the current distortion, which indicates the sector selection part performs well.
2) When the NP voltage deviation happens, the imbalance can be restored quickly with the proposed method. Due to adopting multiple vectors, the input currents gain a high quality.
3) The FSF-MPC can fix the switching frequency per sampling period, which is beneficial to the design of filter. The FSFO-MPC can optimize the sequence between adjacent sampling period on the basis of FSF-MPC, which is beneficial for reducing the switching loss.
4) The cost function in (16) can achieve the current tracking part. Besides, its results are brought into (15) to determine the candidate subsectors. Moreover, they can also be calculated in (20) to obtain the duty ratios of the three candidate vectors to generate a five-segment sequence. Thus, the proposed method gains high integrity and unity for the Vienna rectifier.

Therefore, it is observed that the two MPC strategies proposed in this article can achieve multi control objectives properly to solve the above-mentioned problems, and improve the performance of Vienna rectifier in industrial applications effectively.

References

[1] H. Xu, W. Yao, and S. Shao, "Improved SVPWM schemes for Vienna rectifiers without current distortion," in *Proc. IEEE Energy Convers. Congr. Expo.*, 2017, pp. 3410–3414.
[2] Y. Fu, N. Cui, J. Song, Z. Chen, C. Fu, and C. Zhang, "A hybrid control strategy based on lagging reactive power compensation for Vienna-type rectifier," *IEEE Trans. Transp. Electrific.*, vol. 7, no. 2, pp. 825–837, Jun. 2021.

[3] W. Ding, C. Zhang, F. Gao, B. Duan, and H. Qiu, "A zero-sequence component injection modulation method with compensation for current harmonic mitigation of a Vienna rectifier," *IEEE Trans. Power Electron.*, vol. 34, no. 1, pp. 801–814, Jan. 2019.
[4] J.-H. Park, J.-S. Lee, and K.-B. Lee, "Sinusoidal harmonic voltage injection PWM method for Vienna rectifier with an LCL filter," *IEEE Trans. Power Electron.*, vol. 36, no. 3, pp. 2875–2888, Mar. 2021.
[5] J.-S. Lee and K.-B. Lee, "A novel carrier-based PWM method for Vienna rectifier with a variable power factor," *IEEE Trans. Ind. Electron.*, vol. 63, no. 1, pp. 3–12, Jan. 2016.
[6] J. Lee and K. Lee, "Carrier-based discontinuous PWM method for Vienna rectifiers," *IEEE Trans. Power Electron.*, vol. 30, no. 6, pp. 2896–2900, Jun. 2015.
[7] M. Leibl, J. W. Kolar, and J. Deuringer, "Sinusoidal input current discontinuous conduction mode control of the VIENNA rectifier," *IEEE Trans. Power Electron.*, vol. 32, no. 11, pp. 8800–8812, Nov. 2017.
[8] C. Xia, T. Liu, T. Shi, and Z. Song, "A simplified finite-control-set model-predictive control for power converters," *IEEE Trans. Ind. Inform.*, vol. 10, no. 2, pp. 991–1002, May 2014.
[9] K. Antoniewicz, M. Jasinski, M. P. Kazmierkowski, and M. Malinowski, "Model predictive control for three-level four-leg flying capacitor converter operating as shunt active power filter," *IEEE Trans. Ind. Electron.*, vol. 63, no. 8, pp. 5255–5262, Aug. 2016.
[10] N. N. Nam, N. D. Nguyen, C. Yoon, M. Choi, and Y. I. Lee, "Voltage sensorless model predictive control for a grid-connected inverter with LCL filter," *IEEE Trans. Ind. Electron,* vol. 69, no. 1, pp. 740–751, Jan. 2022.
[11] P. Chaber and M. Ławryńczuk, "AutoMATiC: Code generation of model predictive control algorithms for microcontrollers," *IEEE Trans. Ind. Inform.*, vol. 16, no. 7, pp. 4547–4556, Jul. 2020.
[12] P. Chaber and M. Ławryńczuk, "Fast analytical model predictive controllers and their implementation for STM32 ARM microcontroller," *IEEE Trans. Ind. Inform.*, vol. 15, no. 8, pp. 4580–4590, Aug. 2019.
[13] Y. Yang, H. Wen, M. Fan, M. Xie, and R. Chen, "Fast finite-switching-state model predictive control method without weighting factors for T-type three-level three-phase inverters," *IEEE Trans. Ind. Inform.*, vol. 15, no. 3, pp. 1298–1310, Mar. 2019.
[14] S. A. Davari, V. Nekoukar, C. Garcia, and J. Rodriguez, "Online weighting factor optimization by simplified simulated annealing for finite set predictive control," *IEEE Trans. Ind. Inform.*, vol. 17, no. 1, pp. 31–40, Jan. 2021.
[15] J. Lee and K. Lee, "Predictive control of Vienna rectifiers for PMSG systems," *IEEE Trans. Ind. Electron.*, vol. 64, no. 4, pp. 2580–2591, Apr. 2017.
[16] Y. Yang et al., "Improved model predictive current control for three-phase three-level converters with neutral-point voltage ripple and common mode voltage reduction," *IEEE Trans. Energy Convers.*, vol. 36, no. 4, pp. 3053–3062, Dec. 2021.
[17] T. Liu, A. Chen, C. Qin, J. Chen, and X. Li, "Double vector model predictive control to reduce common-mode voltage without weighting factors for three-level inverters," *IEEE Trans. Ind. Electron.*, vol. 67, no. 10, pp. 8980–8990, Oct. 2020.
[18] H. Zhang, C. Zhang, X. Xing, C. Liu, X. Li, and B. Zhang, "Three-layer double-vector model predictive control strategy for current harmonic reduction and neutral-point voltage balance in Vienna rectifier," *IEEE Trans. Transp. Electrific.*, vol. 8, no. 1, pp. 251–262, Mar. 2022.
[19] A. Mora, R. Cárdenas-Dobson, R. P. Aguilera, A. Angulo, F. Donoso, and J. Rodriguez, "Computationally efficient cascaded optimal switching sequence MPC for grid-connected three-level NPC converters," *IEEE Trans. Power Electron.*, vol. 34, no. 12, pp. 12464–12475, Dec. 2019.
[20] S. Vazquez, P. Acuna, R. P. Aguilera, J. Pou, J. I. Leon, and L. G. Franquelo, "DC-link voltage-balancing strategy based on optimal switching sequence model predictive control for single-phase H-NPC converters," *IEEE Trans. Ind. Electron.*, vol. 67, no. 9, pp. 7410–7420, Sep. 2020.
[21] D. Zhou, L. Ding, and Y. Li, "Two-stage optimization-based model predictive control of 5L-ANPC converter-fed PMSM drives," *IEEE Trans. Ind. Electron.*, vol. 68, no. 5, pp. 3739–3749, May 2021.
[22] K. K. Monfared, Y. Neyshabouri, A. Miremad, S. Ahmadi, and H. Iman-Eini, "Optimal switching-sequence-based model predictive control for a hybrid multilevel STATCOM," *IEEE Trans. Ind. Electron.*, vol. 69, no. 10, pp. 9952–9960, Oct. 2022.
[23] Y. Li, F. Diao, Y. Zhao, and H. A. Mantooth, "A hybrid model predictive control for a seven-level hybrid multilevel converter with independent low-frequency and high-frequency stages," *IEEE Trans. Power Electron.*, vol. 37, no. 5, pp. 5256–5271, May 2022.
[24] F. Donoso, A. Mora, R. Cárdenas, A. Angulo, D. Sáez, and M. Rivera, "Finite-set model-predictive control strategies for a 3L-NPC inverter operating with fixed switching frequency," *IEEE Trans. Ind. Electron.*, vol. 65, no. 5, pp. 3954–3965, May 2018.
[25] Y. Yang et al., "An efficient model predictive control using virtual voltage vectors for three-phase three-level converters with constant switching frequency," *IEEE Trans. Ind. Electron.*, vol. 69, no. 4, pp. 3998–4009, Apr. 2022.
[26] C. Zhang, X. Li, X. Xing, B. Zhang, R. Zhang, and B. Duan, "Modeling and mitigation of resonance current for modified LCL-type parallel inverters with inverter-side current control," *IEEE Trans. Ind. Electron.*, vol. 18, no. 2, pp. 932–942, Feb. 2022.
[27] C. Xia, G. Zhang, Y. Yan, X. Gu, T. Shi, and X. He, "Discontinuous space vector PWM strategy of neutral-point-clamped three-level inverters for output current ripple reduction," *IEEE Trans. Power Electron.*, vol. 32, no. 7, pp. 5109–5121, Jul. 2017.

Chang Liu (Student Member, IEEE) was born in Shandong, China, in 1996. He received the B.S. degree in automation from Hefei University of Technology, Hefei, China, in 2019, and the M.S. degree in automation in 2022 from the School of Control Science and Engineering, Shandong University, Jinan, China, where he is currently working toward the Ph.D. degree.

His current research interests include model predictive control and multilevel converters.

Xiangyang Xing (Member, IEEE) was born in Rizhao, China, in 1985. He received the B.S. degree in automation and the M.S. degree in control theory and application from Qufu Normal University, Qufu, China, in 2009 and 2012, respectively, and the Ph.D. degree in electrical engineering from Shandong University, Jinan, China, in 2016.

From 2017 to 2019, he was a Postdoctoral Research Fellow with Shandong University, Shandong, China. In 2019, he joined Shandong University, where he is currently an Associate Professor with the School of Control Science and Engineering. His current research interests include multilevel converters, power conversion, and renewable power generation.

Chunshui Du (Member, IEEE) was born in Shandong, China, in 1973. He received the B.Sc., M.Sc., and Ph.D. degrees from Shandong University, Jinan, China, in 1997, 2002, and 2011, respectively.

In 2003, he joined the School of Control Science and Engineering, Shandong University. In 2014, he was a Visiting Scholar with the University of Tennessee, Knoxville, TN, USA. He has been involved in research on alternative energy generation, multilevel converters, high-frequency soft-switching power converters, and microgrid control technology.

Boxue Zhang was born in Hebei, China, in 1997. She received the B.S. degree from Yanshan University, Qinhuangdao, China, in 2019, and the M.S. degree from Shandong University, Jinan, China, in 2022, both in electrical engineering. She is currently working toward the Ph.D. degree with The Chinese University of Hong Kong, Hong Kong.

Her current research interests include multilevel inverters and renewable power generation

Chenghui Zhang (Senior Member, IEEE) was born in Shandong, China, in 1963. He received the bachelor's and master's degrees in automation engineering from Shandong University of Technology, Jinan, China, in 1985 and 1988, respectively, and the Ph.D. degree in control theory and operational research from Shandong University, Jinan, China, in 2001.

In 1988, he joined Shandong University, where he is currently a Professor of the School of Control Science and Engineering, Shandong University, the Chief Manager of the Power Electronic Energy-saving Technology & Equipment Research Center of Education Ministry, a Specially Invited Cheung Kong Scholars Professor by the China Ministry of Education, and a Taishan Scholar Special Adjunct Professor. He is also one of the State-level candidates of "the New Century National Hundred, Thousand and Ten Thousand Talent Project," the Academic Leader of the Innovation Team of the Ministry of Education, and the Chief Expert of the National "863" high technological planning. His research interests include optimal control of engineering, power electronics and motor drives, energy-saving techniques, and time-delay systems.

Frede Blaabjerg (Fellow, IEEE) received the Ph.D. degree in electrical engineering from Aalborg University, Aalborg, Denmark, in 1995.

From 1987 to 1988, he was with ABB-Scandia, Randers, Denmark. He became an Assistant Professor in 1992, an Associate Professor in 1996, and a Full Professor of power electronics and drives in 1998 with AAU Energy. In 2017, he became a Villum Investigator. He is honoris causa with University Politehnica Timisoara (UPT), Romania, in 2017 and Tallinn Technical University (TTU), Estonia, in 2018. He has authored or coauthored more than 600 journal papers in the fields of power electronics and its applications. He is the coauthor of four monographs and an editor of ten books in power electronics and its applications. His current research interests include power electronics and its applications such as in wind turbines, PV systems, reliability, harmonics, and adjustable speed drives.

Dr. Blaabjerg received 38 IEEE Prize Paper Awards, the IEEE PELS Distinguished Service Award in 2009, the EPE-PEMC Council Award in 2010, the IEEE William E. Newell Power Electronics Award in 2014, the Villum Kann Rasmussen Research Award in 2014, the Global Energy Prize in 2019, and the 2020 IEEE Edison Medal. He was the Editor-in-Chief for the IEEE TRANSACTIONS ON POWER ELECTRONICS from 2006 to 2012. He has been a Distinguished Lecturer for the IEEE Power Electronics Society from 2005 to 2007 and for the IEEE Industry Applications Society from 2010 to 2011 as well as from 2017 to 2018. In 2019–2020, he served as the President of the IEEE Power Electronics Society. He has been the Vice-President of the Danish Academy of Technical Sciences. He is nominated in 2014–2021 by Thomson Reuters to be among the most 250 cited researchers in Engineering in the world.